Atomic-scale structural and electronic properties of SrTiO_{3}/GaAs interfaces: A combined STEM-EELS and first-principles study

Liang Hong, Kunal Bhatnagar, Ravi Droopad, Robert F. Klie, and Serdar Öğüt

Phys. Rev. B **96**, 035311 — Published 26 July 2017

DOI: 10.1103/PhysRevB.96.035311

Atomic-scale structural and electronic properties of $SrTiO_3$/GaAs interfaces: A combined STEM-EELS and first-principles study

Liang Hong,[1] Kunal Bhatnagar,[2] Ravi Droopad,[2] Robert F. Klie,[1] and Serdar Öğüt[1]

[1]*Department of Physics, University of Illinois at Chicago, Chicago, IL 60607, USA*

[2]*Ingram School of Engineering, Texas State University, San Marcos, TX 78666, USA*

(Dated: July 7, 2017)

Abstract

The electronic properties of epitaxial oxide thin films grown on compound semiconductors are largely determined by the interfacial atomic structure, as well as the thermodynamic conditions during synthesis. Ferroelectric polarization and Fermi-level pinning in $SrTiO_3$ films have been attributed to the presence of oxygen vacancies at the oxide/semiconductor interface. Here, we present scanning transmission electron microscopy (STEM) and electron energy-loss spectroscopy (EELS) analysis of GaAs films grown on $SrTiO_3$ combined with first-principles calculations to determine the atomic and electronic structures of the $SrTiO_3$/GaAs interfaces. An atomically abrupt SrO/As interface is observed and the interfacial SrO layer is found to be O-deficient. First-principles density functional theory (DFT) calculations show SrO/Ga and Sr/As interfaces are favorable under O-rich and O-poor conditions, respectively. SrO/Ga interface is reconstructed via the formation of Ga-Ga dimers while Sr/As interface is abrupt and consistent with the experiment. DFT calculations further reveal that intrinsic two-dimensional electron gas (2DEG) forms in both SrO/Ga and Sr/As interfaces and the Fermi level is pinned to the localized 2DEG states. Interfacial O vacancies can enhance the 2DEG density while it is possible for Ga/As vacancies to unpin the Fermi level from the 2DEG states.

I. INTRODUCTION

The properties of a hybrid thin film hetero-structure are often dominated by the interface between the materials that comprise the structure. Extensive research has revealed key mechanisms and material properties that control an interface between chemically similar, isostructural materials. Integrating thin films with dramatically dissimilar chemical bonding, crystal symmetries and electronic structures, represents a promising new approach to engineer novel functional materials. For example, ultrathin $SrTiO_3$ (STO) films grown on Si or GaAs that exhibit ferroelectric properties can facilitate the implementation of optical nonlinearities and carrier modulation at extremely high carrier densities. Successful integration of STO thin film on Si substrate was first demonstrated by McKee *et al.* [1]. Compared to Si, compound semiconductors, such as GaAs, have much higher electron mobility, wider and direct band gap, making them promising for applications in electronics and photonics by directly coupling the polarization of a ferroelectric to the properties of a semiconductor. Perovskite oxide thin films, exhibiting enormous optical nonlinearities, can, therefore, serve as a key component for hybrid semiconductor-photonic systems. However, deposition of perovskite oxides directly with semiconductors is challenging, due to the structural difference and the potential oxidation of semiconductor surface [2]. Since the stability and performance of these hetero-junctions are often governed by atomic-scale defects and interfaces between the two dissimilar materials, an understanding of the interfacial structural and electronic properties is critical.

The STO/GaAs hetero-interfaces have been studied both theoretically and experimentally during the last decade [3–15]. STO thin film was epitaxially deposited on GaAs (001) without any amorphous interfacial layer using molecular beam epitaxy (MBE) method first by Liang *et al.* [3; 4]. A Ti prelayer was used to facilitate the growth of STO on GaAs substrate. Epitaxial STO thin film was found to be rotated by 45° with respect to GaAs so that the lattice mismatch between STO ($a_{\mathrm{STO}} = 3.905$ Å) and GaAs ($a_{\mathrm{GaAs}}/\sqrt{2} = 3.997$ Å) can be minimized to 2.3%. The STO/GaAs interfaces were then characterized using scanning transmission electron microscopy (STEM) imaging at atomic-resolution by Klie *et al.* [5] It was reported that SrO-terminated STO film is epitaxially grown on As-terminated GaAs with atomically sharp interfaces. In addition, STO thin films deposited with and without Ti prelayer on GaAs have structurally identical interfaces. A more detailed characterization

of the atomic and electronic structures of the STO/GaAs interfaces was carried out by Qiao *et al.* [6] using low-energy electron energy-loss spectroscopy (EELS) along with first-principles calculations. By analyzing the O vacancies and Ti concentrations in the STO film and across the interface, it was suggested that without the presence of Ti prelayer, the interfacial As gets oxidized which results in the Fermi-level pinning, while in the presence of Ti prelayer, Ti diffuses into surface GaAs and alleviates the oxidation which unpins the Fermi level. From a computational perspective, there have been few first-principles total energy calculations performed using density functional theory (DFT) to determine the stable structures of the STO/GaAs interfaces. By comparing the formation energies of various interface configurations, the SrO/Ga hetero-structure with Ga-O bonds was found to be the most favorable [12–15], which is consistent with the recent X-ray photoemission spectroscopy characterization of the STO/GaAs interface [9]. However, a more systematic and detailed study with a combination of experimental and theoretical investigations is needed to determine the structure of the STO/GaAs interface. Since GaAs (001) was used experimentally as a substrate with fixed As-termination in the previous STEM-EELS studies, it was not possible to determine the energetic preference of Ga- or As-termination at the interface. This can be potentially solved by depositing GaAs films on STO, which was achieved more than a decade ago by Droopad *et al.* [16; 17], but the atomic structure of this hetero-interface has not yet been characterized. In addition, the effects of atomic-scale interfacial defects on the electronic properties of the hetero-structure, including Fermi-level pinning and band alignment, need to be studied to establish a better understanding of the structure-property relationship of the STO/GaAs interface.

In this work, we present results and analyses of a combined experimental and theoretical study of the STO/GaAs hetero-interfaces at atomic scale. Epitaxial GaAs is grown on Si substrate with a STO buffer layer using MBE method. The STO/GaAs interface in our sample is characterized using atomic-resolution STEM imaging and EELS. (2×2) structural models with various interface compositions are constructed and optimized using first-principles DFT calculations. Our results show that O-deficient SrO layer in contact with As layer is the most favorable interface structure and the experimentally observed interface structure is reproduced in the DFT simulation. Ga-termination is favored over As-termination at the interface under O-rich condition but the GaAs surface is easily oxidized by forming a Ga_2O_3 interlayer. The interface structure is determined by the accommodation of polar discontinu-

ity which is related to the interface composition. Interfacial vacancies are found to play an important role in determining the electronic properties of the hetero-interfaces. The rest of the paper is organized as follows. In Sec. II, we discuss the technical details of the experimental and theoretical methods used in this work. In Sec. III, we present both experimental and theoretical results and analyses of the STO/GaAs interfaces including their energetics, atomic and electronic structures and the effect of interfacial vacancies. Finally, our results are summarized in Sec. IV.

II. METHODS

A. Experimental methods

The sample used in this work is grown using the MBE method. A 10-nm-thick SrO-terminated STO thin film is grown on Si (001) wafer with a 4° miscut in the [110] direction. During the growth, oxygen diffuses through the perovskite STO layer and reacts with the interfacial Si atoms forming a SiO_2 interlayer. The SrO-termination of STO film is achieved by closing the shutter of Ti effusion cell while keeping that of Sr effusion cell open in the oxide MBE chamber. The wafer is then transferred into a second MBE chamber for the growth of III-V semiconductor layer. Simultaneous Ga and As_2 are exposed to the STO surface to form a 1-μm-thick epitaxial GaAs layer. More details about the MBE growth are presented in the Supplemental Materials [18].

Two cross-section samples are polished in two directions that are 90° rotated with respect to each other using standard wedge polishing methods and then thinned down to electron transparency (< 50 nm) using low-energy ($0.5 - 3$ kV) and low-angle ($6° - 10°$) argon ion milling on a liquid-nitrogen-cooled stage to minimize the ion beam damage.

The experimental characterization data are obtained using the aberration-corrected JEOL JEM-ARM200CF scanning transmission electron microscopy (STEM) equipped with a cold field-emission source, which yields an energy resolution of 0.35 eV, and a probe spherical-aberration corrector which allows for 78 pm spatial resolution using an acceleration voltage of 200 kV [19]. The high-angle annular dark-field (HAADF) images are acquired at 200 kV with a convergence semi-angle of 29 mrad and a collection angle from 90 to 170 mrad. The atomic-resolution HAADF images are recorded at magnification of 2×10^7 (pixel size of 0.02

nm) and pixel dwell time of 31 μs. For EELS at 200 kV, a convergence angle of 30 mrad and a collection angle with 35 mrad are used. Energy dispersions of 0.1 eV/channel and 0.3 eV/channel are used for the measurement of Ti $L_{3,2}$-edge and O K-edge, respectively. The atomic-resolution EELS line scan is recorded using pixel size of 0.06 nm and pixel dwell time of $0.5-0.7$ s. The exponential EEL spectrum background is subtracted from each spectrum and the resulting data are normalized with respect to the post edge intensity. No obvious beam damage to the sample is observed during both imaging and EELS collection at 200 kV.

B. Theoretical methods

First-principles calculations are carried out within the framework of DFT using the projector augmented wave method [20], as implemented in Vienna *Ab initio* Simulation Package (VASP) [21], and the exchange-correlation functional of Perdew-Burke-Ernzerhof (PBE) [22]. Plane wave energy cutoff is set as 400 eV. Periodic slabs with (2×2) surface cell, as shown in Fig. 1, are constructed to simulate the STO/GaAs interfaces. The slabs are fully optimized with a maximum force criterion of 10^{-2} eV/Å. $4\times4\times1$ and $12\times12\times1$ Monkhorst-Pack k-point grids are used during structural optimization and density of states (DOS) calculations, respectively.

The computed lattice parameters of bulk STO and GaAs are found to be 3.94 Å and 5.76 Å, respectively. To mimic GaAs growth on STO substrate, we use the in-plane lattice parameter of $a_{\mathrm{GaAs}} = 5.57$ Å $(= \sqrt{2}a_{\mathrm{STO}})$ for GaAs, with a 45° in-plane rotation, to match the lattice parameter of STO. The top surface of GaAs is As layer and is passivated with pseudo-hydrogens to saturate the As dangling bonds [23]. The bottom surface of STO is SrO layer in contact with an out-of-plane vacuum of 8 Å to separate the slabs. The electronic and structural properties of the slabs are well converged with respect to both the k-point sampling and the length of vacuum. Various interface structures, including SrO- or TiO_2-terminated STO and bare Sr- or Ti-terminated STO in contact with Ga- or As-terminated GaAs, are constructed to investigate the STO/GaAs interfacial registry. We use the notation SrO/Ga (Sr/Ga) to denote the interface of fully oxygenated (O-deficient) SrO-terminated STO in contact with Ga-terminated GaAs. Considering all the terminations, we have 8 different interfacial configurations, which are SrO/Ga, TiO_2/Ga, SrO/As, TiO_2/As, Sr/Ga,

Ti/Ga, Sr/As and Ti/As.

The formation energy for a given interfacial configuration is defined as [24]

$$E_{\text{interface}} = E_{\text{slab}} - n_{\text{Sr}}\mu_{\text{Sr}} - n_{\text{Ti}}\mu_{\text{Ti}} - n_{\text{O}}\mu_{\text{O}} - n_{\text{Ga}}\mu_{\text{Ga}} - n_{\text{As}}\mu_{\text{As}}, \quad (1)$$

where E_{slab} is the total energy of the corresponding slab, n_i (i = Sr, Ti, O, Ga and As) is the number of atoms or units of type i in the slab, and μ_i is the corresponding chemical potential. The chemical potentials in Eq. (1) are subject to the constraints of equilibrium with bulk STO and GaAs. Additional constraints are used to prevent formation of secondary phases including TiO_2, Ti_2O_3, $Sr_6Ti_5O_{16}$ and Ga_2O_3 [12; 25; 26]. More details about the proposed interface structures, constraints of chemical potentials and band alignment are presented in the Supplemental Materials [18].

III. RESULTS AND DISCUSSION

A. Experimental characterization of the interface

The atomic-resolution HAADF images of our sample taken from cross-sections in two directions that are rotated 90° with respect to each other are displayed in Fig. 2. Figure 2(a), with STO [010]||GaAs [110] epitaxy, shows full GaAs dumbbell structure at the interface, while Fig. 2(c), with STO [100]||GaAs [1$\bar{1}$0] epitaxy, shows half GaAs dumbbell structure at the interface. Both images exhibit a sharp interface between STO and GaAs in 1× periodicity without any surface reconstruction or amorphous interlayer. The elements can be characterized by the intensity contrast of each atomic column in the HAADF images since the HAADF intensity is directly correlated to the atomic number. From the intensity line profiles shown in Fig. 2(b) and (d), we can clearly see that STO films are terminated by SrO layer while GaAs is terminated by As. The interfacial As atoms are located above the oxygen sites in the SrO, and the GaAs dumbbells are in excellent epitaxy with respect to SrO or TiO_2 columns in the out-of-plane direction.

For Ti oxides, it is known that the energy-loss near-edge fine-structures in the Ti $L_{3,2}$-edge can reflect the valence state, coordination and site geometry of Ti [27], providing fundamental information on cation ordering and defect clustering such as O vacancies [28]. Therefore, atomic-resolution EEL spectra of Ti $L_{3,2}$-edge are taken from the first four TiO_2 layers at the STO/GaAs interface and compared with that in bulk STO to examine the

near-interface Ti valence and O concentration. As shown in Fig. 3(a), the Ti $L_{3,2}$-edge of the second to fourth TiO_2 layers exhibit four prominent peaks originating from the splitting of $3d^0$ states into t_{2g} and e_g components, which corresponds to a Ti^{4+} valence. In the first TiO_2 layer, the intensity of the t_{2g} peaks significantly decreases and the positions of e_g peaks shift to lower energies, which indicates a decrease of Ti valence from 4+ to a mixture of 3+ and 4+ [28; 29]. The decrease of Ti valence near the interface can be attributed to the interfacial O vacancies. Moreover, the t_{2g}-e_g splitting in both the L_3- and L_2-edges reduces near the interface compared to the bulk spectrum, as a result of the increased TiO_6 octahedral distortion due to O vacancies and the ferroelectric polarization induced by the polar GaAs (001) surface.

To further confirm the interfacial O vacancies, atomic-resolution EEL spectra of O K-edge are taken from the first four SrO layers at the STO/GaAs interface. In Fig. 3(b), it is clearly noticeable that the near-edge fine-structure of O K-edge fades in the first SrO layer, due to the destruction of long-range order in the O sublattice and the presence of interfacial O vacancies [30]. The three featured peaks (labeled as a, b and c) for STO bulk are all observed in the second to fourth SrO layers; however, the intensity of peak a, which is assigned to the hybridization of O $2p$ with Ti $3d(t_{2g})$, decreases from fourth to second SrO layer, suggesting that Ti t_{2g} orbital is partially occupied near the interface.

In summary, when GaAs is deposited on STO, As atoms are favored to be in contact with an O-deficient SrO surface to form an atomically abrupt STO/GaAs interface without surface reconstruction. The observed interface structure is consistent with the HAADF images of STO thin film grown on GaAs substrate in the previous studies [5; 6; 31]. Therefore, the experimentally favorable configuration of STO/GaAs hetero-interfaces is O-deficient SrO layer in contact with As layer and this configuration is independent of which one is the substrate material.

B. Theoretical characterization of the interface

1. Stability of the interface structures

First-principles DFT calculations are carried out to further explore the structural and electronic properties of the STO/GaAs interfaces observed in the experiment. All the pro-

posed interface structures are fully relaxed in the geometry optimization. As a result, some of the initial structures with different interfacial configurations turn into the same structure. In the following discussion, we only focus on the most stable geometry for each interfacial composition.

The formation energies of interface structures with different compositions are compared by the ternary phase diagrams shown in Fig. 4. The phase diagrams exhibit similar landscapes for Ga-rich and As-rich conditions. The SrO/Ga and Sr/As interfaces (the blue and red areas in the phase diagram) turn out to be the most stable structures under O-rich and O-poor conditions, respectively. The results show that SrO layer either with or without O vacancies is favored over TiO_2 layer at the STO/GaAs interface, which is consistent with the previous experimental findings that no Ti is observed at the interface even though a Ti thin layer was pre-deposited between the GaAs and STO during the MBE growth in earlier studies [5; 6]. The phase diagram illustrates a critical value of the oxygen chemical potential, $\mu_O = -4.67$ eV (Ga-rich) and $\mu_O = -4.05$ eV (As-rich), for the switching of the preferred interfacial layer from As to Ga. We also examine the formation energies using the lattice parameter of bulk GaAs ($a_{GaAs} = 5.76$ Å) for the slabs to mimic the situation of STO grown on GaAs substrate. The phase diagrams are found to be independent of the deposition sequence (i.e. GaAs on STO or STO on GaAs).

Considering the oxygen flux used in the deposition of STO, the GaAs (001) can be easily oxidized by formation of Ga_2O_3 on the surface [12; 26]. The maximal chemical potential of oxygen for an interface without forming Ga_2O_3 is calculated as $\mu_O^{max} = -3.94$ eV (Ga-rich) and $\mu_O^{max} = -3.51$ eV (As-rich). Imposing the chemical potential constraint to avoid precipitation of Ga_2O_3, the allowed region where GaAs can be epitaxially deposited on STO is restricted into a small area in the O-poor and Sr-rich corner of the phase diagram, which is dominated by Sr/As interface. According to the calculated phase diagram, no thermodynamically stable and atomically abrupt STO/GaAs hetero-interface can be obtained in the O-rich condition. Considering the normal MBE growth condition for oxygen which is 300°C to 500°C at 10^{-8} mbar, the allowed O chemical potential is limited to the range of -1.20 eV to -1.78 eV (calculated using the method in Ref. [32]), which is within the range of Ga_2O_3 formation discussed above. Therefore, when STO is directly deposited on GaAs substrate with oxygen flux, there should, at equilibrium, always be a layer of Ga_2O_3 forming prior to the STO. In order to obtain an abrupt interface, the oxygen flux should be turned off during

the growth of the interface. This kinetic inhibition of Ga_2O_3 is similar to that of SiO_2 in the STO/Si interfaces [33]. On the other hand, when depositing GaAs on STO, oxygen is mainly provided by the STO substrate; thus, the first GaAs layer is determined by the O concentration at the STO surface.

2. Atomic and electronic structures of the interfaces

In the following discussion, we mainly focus on the two energetically favorable interface structures, which are SrO/Ga and Sr/As. Figure 5 shows the relaxed structures of the two interfaces, which exhibit different patterns. In the SrO/Ga interface structure, we find a $c(2\times2)$ interface reconstruction of Ga atoms by forming Ga dimers and Ga-O bonds as shown in Fig. 5(a) and (b). The stability of the $c(2\times2)$ reconstruction has been confirmed by testing larger unit cells such as (2×4) and (4×2), known as the favorable size of GaAs surface reconstruction [34]. In the Sr/As interface structure, there is no surface reconstruction, where the (1×1) surface unit cell is preserved, and interfacial As atoms sit on the top of the Sr hollow sites (O vacancies) as shown in Fig. 5(c) and (d).

The STO/GaAs hetero-structure can be divided into alternating (001) planes of SrO, TiO_2, Ga and As. SrO and TiO_2 layers are charge neutral while Ga and As layers take on $+3$ and -3 charges, respectively. Therefore, the STO/GaAs interface has a polar discontinuity, which has to be compensated. For Ga-termination, each Ga atom has $1.5e^-$ in its dangling bonds at the interface, while for SrO-termination, each Sr atom can provide $2e^-$ for each O to fill the O $2p$ orbital. Thus, in the reconstructed $c(2 \times 2)$ SrO/Ga interface cell (with 2 atoms of each species in the surface unit cell), the electropositive elements (Ga and Sr) can provide a total of $7e^-$ while the electronegative element (O) only needs $4e^-$. Since Sr is not able to change its valence state, the interface must reconstruct to accommodate the polar discontinuity. The GaAs surface is then reconstructed by forming a Ga-Ga dimer which consumes $2e^-$ and leaves $1e^-$ (i.e. $0.5e^-$ per (1×1) unit cell). For As-termination, each As atom needs $1.5e^-$ to saturate its dangling bonds, which can be provided by the Sr atom in the Sr layer. The remaining $0.5e^-$ of Sr atom transfers to Ti atom in the TiO_2 layer underneath, lowering the valence of Ti from 4+ to 3.5+. The polar discontinuity is then accommodated by the creation of electrical dipole in the first STO unit cell. Thus, the Sr/As interface structure is abrupt without GaAs reconstruction, which is in good agreement with

the interface observed in our STEM images, and the microscopic explanation of interfacial charge distribution can be also confirmed by the EEL spectra. The reconstruction of GaAs is found in other interface structures which are not presented in the phase diagram, such as the Sr/Ga and SrO/As interfaces (shown in the Supplemental Materials [18]).

The projected density of states (DOS) on each element in each STO and GaAs unit cell are plotted for the SrO/Ga and Sr/As interfaces as shown in Fig. 6. Both interfaces are metallic with the Fermi level pinned to the conduction band minimum (CBM) of STO and the states at Fermi level are mainly contributed by Ti $3d$ states. In order to verify that the observed Fermi level pinning is not an artifact of the DFT band-gap underestimation [35], we perform PBE + U method with the effective Hubbard correction ($U = 2.0,\ 4.0,\ 6.0$ and 8.0 eV) to Ti $3d$ states. The results show that even though the band gap of STO increases as U increases, the Fermi level remains pinned to the CBM of STO with occupied Ti $3d$ states. Therefore, the Fermi level pinning is physically meaningful in our calculations. The details of the PBE + U calculations are presented in the Supplemental Materials [18]. The localized metallic Ti $3d$ states at the CBM of STO are also found in interfaces without O vacancies, indicating that O vacancies are not the main source of these electrons. They can be attributed to the formation of two-dimensional electron gas (2DEG), which has been extensively demonstrated in the STO-based complex oxide hetero-interfaces and vacuum-cleaved STO surface [36–44]. To further explore the 2DEG at the STO/GaAs interfaces, the charge density of the 2DEG is calculated by integrating the DOS of the Ti occupied states, and plotted as a function of TiO_2 layers as shown in Fig. 7. We can see that the occupied states in the CBM of STO exhibit a strong 2D character consisting mostly of Ti d_{xy} states. As explained before, both the SrO/Ga and Sr/As interfaces have extra $0.5e^-$ per (1×1) unit cell which corresponds to a charge density of $\sim 3.0 \times 10^{14}$ cm^{-2}, donated from the electropositive elements and transfered to the unoccupied Ti $3d$ orbitals in the first TiO_2 layer; however, the computed charge density at the interface is much lower than that value since the 2DEG can spread over several layers into the bulk region [38]. It is noteworthy that Sr/As structure has a higher charge density than the SrO/Ga structure in the first TiO_2 layer, suggesting that O vacancies are able to enhance the 2DEG at the interface. Moreover, we find that the first and last TiO_2 layers have higher charge density than the middle layers, indicating the formation of 2DEG at both STO/GaAs interface and vacuum/STO surface.

In addition, band alignment across the SrO/Ga and Sr/As interfaces is examined with

results illustrated in Fig. 8, in order to obtain the macroscopic electronic properties of the hetero-sturctures. For the SrO/Ga interface, the conduction and valence band offsets are calculated as $\Delta E_{\rm c} = -0.15$ eV and $\Delta E_{\rm v} = 1.68$ eV, corresponding to a type I hetero-structure. For the Sr/As interface, the conduction and valence band offsets are obtained as $\Delta E_{\rm c} = 0.57$ eV and $\Delta E_{\rm v} = 2.40$ eV, corresponding to a type II hetero-structure, which is in excellent agreement with the experimental values (0.6 ± 0.1 eV and 2.5 ± 0.1 eV) [4]. The difference of band offsets between the two structures is due to the higher electrostatic potential of GaAs with respect to STO in Sr/As interface than that in SrO/Ga interface, as can be seen in Fig. 8.

3. Vacancies at the interfaces

From the previous discussion, we know that O vacancies play an important role in determining the structural properties of the STO/GaAs interfaces. In this section, we consider two types of interfacial defects, which are O vacancies in the first SrO layer and Ga/As vacancies in the first Ga/As layer, to gain further insights into the influence of defects on structural and electronic properties. For both Ga- and As-terminated GaAs, O vacancies are considered in the interfacial $SrO_{1-\delta}$ layer with different vacancy concentrations $\delta = 0.25, 0.5$ and 0.75. For SrO-terminated STO, Ga or As vacancies are created in the interfacial $Ga_{1-\theta}$ or $As_{1-\theta}$ layer with vacancy concentrations $\theta = 0.25, 0.5$ and 0.75. For Sr-terminated STO, only As vacancies are considered in the interfacial $As_{1-\theta}$ layer with vacancy concentrations $\theta = 0.25, 0.5$ and 0.75. Other mixed O and Ga/As vacancies are not considered in this work due to the complexity of the possible interfacial configurations.

The proposed structures are fully relaxed and their electronic structures are calculated. All the structures with vacancies are found to be energetically less stable than the original SrO/Ga and Sr/As interfaces; nevertheless, studying the electronic behavior of these vacancies is important for understanding the interface structures and tailoring their properties. Since the metallicity of the STO/GaAs hetero-structure is determined by the valence and conduction states in the interfacial layers, the projected DOS on each element in the first STO and GaAs unit cells at the interface are plotted for the considered structures with vacancies in Fig. 9. Only the $SrO/As_{0.5}$ interface exhibits semiconducting behavior with a sizable band gap, all the other interfaces are metallic. For $SrO_{1-\delta}$/Ga(As) ($\delta = 0.25, 0.5, 0.75$) in-

terfaces, the Fermi level is always pinned to the CBM of STO. However, O vacancies induce extra dangling Ga or As states at valence band maximum (VBM) of GaAs, which reduces the band gap of GaAs at the interface. The similar pinning behavior is also reported in the STO/Si hetero-interfaces [45; 46]. For $SrO/Ga(As)_{1-\theta}$ ($\theta = 0.25, 0.5, 0.75$) interfaces, the Fermi level can be unpinned from the CBM of STO and shifts towards the VBM as vacancy concentration increases. However, Ga and As vacancies result in extra dangling As and Ga states at Fermi level. In the case of $SrO/As_{0.5}$, the dangling states at GaAs surface can be eliminated and the Fermi level can be unpinned from STO, making the interface semiconducting. For the experimentally observed Sr/As interface with As vacancies, the Fermi level is always pinned to the CBM of STO regardless of the vacancy concentration. From these observations, we can conclude that the 2DEG in STO is intrinsic to the STO/GaAs interface and can be also contributed by O vacancies; however, it is possible for Ga or As vacancies to unpin the Fermi level from the localized 2DEG states. Both O and Ga/As vacancies will introduce more occupied Ga/As states near Fermi level, which reduces the band gap at the interface or makes the interface metallic.

IV. SUMMARY

We study the structural and electronic properties of STO/GaAs heterointerfaces using STEM-EELS and first-principles calculations. GaAs thick layer is grown on STO thin film on Si substrate by MBE method to find out the interfacial configuration to complement the previous studies of STO thin films grown on GaAs substrate. The interface is characterized using atomic-resolution HAADF imaging and EELS techniques. We observe an atomically abrupt interface between STO and GaAs with the interfacial configuration of O-deficient SrO layer in contact with As layer, which is identical with that of STO thin film deposited on GaAs substrate. (2×2) structural model of various interfacial compositions with regard to SrO, TiO_2, Sr, Ti, Ga and As terminations are constructed and fully relaxed using first-principle DFT calculations. Energetic stability of all the proposed interface structures are compared in formation energy phase diagrams. Two interfaces, with configurations SrO/Ga and Sr/As, are found to be energetically favorable under O-rich and O-poor conditions, respectively. The phase diagram also indicates that Ga-terminated GaAs surface is easily oxidized, resulting in a Ga_2O_3 interlayer. In the relaxed structure of SrO/Ga interface,

GaAs surface is reconstructed via the formation of Ga-Ga dimers and Ga-O bonds, while the relaxed structure of Sr/As exhibits an abrupt interface without surface reconstruction, which is consistent with the experimentally observed structure. The driving force of interface reconstruction is the accommodation of interface polar discontinuity and the presence of interfacial O vacancies is crucial to obtain an abrupt interface. Both of the two interfaces are metallic with a 2DEG of $0.5e^-$ per (1×1) unit cell localized at the bottom of Ti conduction band. Macroscopic band alignment analysis reveals that the SrO/Ga interface is a type I hetero-structure while Sr/As interface is a type II hetero-structure in agreement with the experiment. The electronic properties of the STO/GaAs interfaces are further studied by examining the effects of O and Ga/As vacancies with different concentrations at the first SrO and Ga/As layers. The results show that the 2DEG in STO is intrinsic to the STO/GaAs interface and can be enhanced by O vacancies; however, it is possible for Ga or As vacancies to unpin the Fermi level from the localized 2DEG states. Experimental studies of the occurrence of the predicted 2DEG will be the subject of our future research. Our results present a detailed understanding of the structural and electronic properties of STO/GaAs hetero-interfaces, which can be useful for future integration and designs of metal-oxide-semiconductor devices with advanced functions.

ACKNOWLEDGMENTS

This work was supported by the National Science Foundation (Grant No. DMR-1408427) and partially used resources of the National Energy Research Scientific Computing Center, a DOE Office of Science User Facility supported by the Office of Science of the U.S. Department of Energy under Contract No. DE-AC02-05CH11231. The acquisition of UIC JEOL JEM ARM200CF is supported by an MRI-R^2 grant from the National Science Foundation (Grant No. DMR-0959470). This work also made use of instruments in the Electron Microscopy Service and the High Performance Computing Clusters at Research Resources Center, UIC.

---

[1] R. McKee, F. Walker, and M. Chisholm, Phys. Rev. Lett. **81**, 3014 (1998).

[2] D. J. Smith, H. Wu, S. Lu, T. Aoki, P. Ponath, K. Fredrickson, M. D. McDaniel, E. Lin, A. B. Posadas, A. A. Demkov, J. Ekerdt, and M. R. McCartney, J. Mater. Res. **32**, 912 (2017).

[3] Y. Liang, J. Kulik, T. Eschrich, R. Droopad, Z. Yu, and P. Maniar, Appl. Phys. Lett. **85** (2004).

[4] Y. Liang, J. A. Curless, and D. E. McCready, Appl. Phys. Lett. **86** (2005).

[5] R. Klie, Y. Zhu, E. Altman, and Y. Liang, Appl. Phys. Lett. **87**, 3106 (2005).

[6] Q. Qiao, R. F. Klie, S. Öğüt, and J. Idrobo, Phys. Rev. B **85**, 165406 (2012).

[7] Z. Wu, W. Huang, K.-h. Wong, and J. Hao, J. Appl. Phys. **104**, 1 (2008).

[8] X. Wei, W. Huang, Z. Yang, and J. Hao, Scripta Mater. **65**, 323 (2011).

[9] R. Contreras-Guerrero, J. Veazey, J. Levy, and R. Droopad, Appl. Phys. Lett. **102**, 012907 (2013).

[10] L. Louahadj, R. Bachelet, P. Regreny, L. Largeau, C. Dubourdieu, and G. Saint-Girons, Thin Solid Films **563**, 2 (2014).

[11] B. Meunier, R. Bachelet, G. Grenet, C. Botella, P. Regreny, L. Largeau, J. Penuelas, and G. Saint-Girons, J. Cryst. Growth **433**, 139 (2016).

[12] F. Bottin and F. Finocchi, Phys. Rev. B **76**, 165427 (2007).

[13] J. Wang, X. Wu, and D. Bai, EPL-Europhys. Lett. **86**, 46008 (2009).

[14] L. Hong, S. Öğüt, and R. Klie, Microsc. Microanal. **21**, 1647 (2015).

[15] J. Gatabi, K. Lyon, S. Rahman, M. Caro, J. Rojas-Ramirez, J. Cott-Garcia, R. Droopad, and B. Lee, Microelectron. Eng. **147**, 117 (2015).

[16] R. Droopad, "Growth of compound semiconductor structures on patterned oxide films and process for fabricating same," (2004), uS Patent 6,673,646.

[17] K. Eisenbeiser, R. Emrick, R. Droopad, Z. Yu, J. Finder, S. Rockwell, J. Holmes, C. Overgaard, and W. Ooms, IEEE Electr. Device L. **23**, 300 (2002).

[18] See Supplemental Material at URL for details of the experimental and theoretical methods, which includes Ref. [47–51].

[19] R. Klie, A. Gulec, Z. Guo, T. Paulauskas, Q. Qiao, R. Tao, C. Wang, K. Low, A. Nicholls, and P. Phillips, Cryst. Res. and Technol. **49**, 653 (2014).

[20] G. Kresse and D. Joubert, Phys. Rev. B **59**, 1758 (1999).

[21] G. Kresse and J. Furthmüller, Comp. Mater. Sci. **6**, 15 (1996).

[22] J. P. Perdew, K. Burke, and M. Ernzerhof, Phys. Rev. Lett. **77**, 3865 (1996).

[23] S. Zhang and S.-H. Wei, Phys. Rev. Lett. **92**, 086102 (2004).

[24] G.-X. Qian, R. M. Martin, and D. Chadi, Phys. Rev. B **38**, 7649 (1988).

[25] C. S. Hellberg, K. E. Andersen, H. Li, P. Ryan, and J. Woicik, Phys. Rev. Lett. **108**, 166101 (2012).

[26] H. Wieder, J. Vac. Sci. Technol. **15**, 1498 (1978).

[27] F. De Groot, M. Figueiredo, M. Basto, M. Abbate, H. Petersen, and J. Fuggle, Phys. Chem. Miner. **19**, 140 (1992).

[28] E. Stoyanov, F. Langenhorst, and G. Steinle-Neumann, Am. Mineral. **92**, 577 (2007).

[29] D. A. Muller, N. Nakagawa, A. Ohtomo, J. L. Grazul, and H. Y. Hwang, Nature **430**, 657 (2004).

[30] N. Browning, J. Buban, H. Moltaji, S. Pennycook, G. Duscher, K. Johnson, R. Rodrigues, and V. Dravid, Appl. Phys. Lett. **74**, 2638 (1999).

[31] Q. Qiao, Y. Zhang, R. Contreras-Guerrero, R. Droopad, S. T. Pantelides, S. J. Pennycook, S. Ogut, and R. F. Klie, Appl. Phys. Lett. **107**, 201604 (2015).

[32] K. Reuter and M. Scheffler, Phys. Rev. B **65**, 035406 (2001).

[33] A. Kolpak and S. Ismail-Beigi, Phys. Rev. B **83**, 165318 (2011).

[34] M. Pashley, Phys. Rev. B **40**, 10481 (1989).

[35] C. Wang and W. Pickett, Phys. Rev. Lett. **51**, 597 (1983).

[36] A. Ohtomo and H. Hwang, Nature **427**, 423 (2004).

[37] J. N. Eckstein, Nature Mater. **6**, 473 (2007).

[38] Z. S. Popović, S. Satpathy, and R. M. Martin, Phys. Rev. Lett. **101**, 256801 (2008).

[39] N. Nakagawa, H. Y. Hwang, and D. A. Muller, Nature Mater. **5**, 204 (2006).

[40] S. Thiel, G. Hammerl, A. Schmehl, C. Schneider, and J. Mannhart, Science **313**, 1942 (2006).

[41] A. Brinkman, M. Huijben, M. Van Zalk, J. Huijben, U. Zeitler, J. Maan, W. Van der Wiel, G. Rijnders, D. Blank, and H. Hilgenkamp, Nature Mater. **6**, 493 (2007).

[42] W. Siemons, G. Koster, H. Yamamoto, W. A. Harrison, G. Lucovsky, T. H. Geballe, D. H. Blank, and M. R. Beasley, Phys. Rev. Lett. **98**, 196802 (2007).

[43] A. Kalabukhov, R. Gunnarsson, J. Börjesson, E. Olsson, T. Claeson, and D. Winkler, Phys. Rev. B **75**, 121404 (2007).

[44] A. Santander-Syro, O. Copie, T. Kondo, F. Fortuna, S. Pailhes, R. Weht, X. Qiu, F. Bertran, A. Nicolaou, A. Taleb-Ibrahimi, *et al.*, Nature **469**, 189 (2011).

[45] I. N. Yakovkin and M. Gutowski, Phys. Rev. B **70**, 165319 (2004).

[46] A. Kolpak and S. Ismail-Beigi, Phys. Rev. B **85**, 195318 (2012).

[47] Y. Wei, X. Hu, Y. Liang, D. Jordan, B. Craigo, R. Droopad, Z. Yu, A. Demkov, J. L. Edwards Jr, and W. J. Ooms, J. Vac. Sci. Technol. B Microelectron Nanometer Struct. **20**, 1402 (2002).

[48] R. Droopad, Z. Yu, H. Li, Y. Liang, C. Overgaard, A. Demkov, X. Zhang, K. Moore, K. Eisenbeiser, M. Hu, *et al.*, J. Crys. Growth **251**, 638 (2003).

[49] T. Sands, J. Washburn, and R. Gronsky, Mater. Lett. **3**, 247 (1985).

[50] A. Baldereschi, S. Baroni, and R. Resta, Phys. Rev. Lett. **61**, 734 (1988).

[51] C. G. Van de Walle and R. M. Martin, Phys. Rev. B **34**, 5621 (1986).

FIG. 1. (Color online) Ball-and-stick model of the (2×2) STO/GaAs interfaces in three-dimensional view. The top surface of GaAs is passivated by pseudo-hydrogen atoms and the bottom surface of STO is in contact with vacuum.

FIG. 2. (Color online) Atomic-resolution HAADF images of the STO/GaAs interface from two different views which are 90° rotated: (a) the STO [010]||GaAs [110] epitaxy with full GaAs dumbbell structure at the interface and (c) the STO [100]||GaAs [$1\bar{1}0$] epitaxy with half GaAs dumbbell structure at the interface. The images are taken from dislocation-free areas and filtered using Average Background Subtraction filter within Gatan Digital Micrograph. (b) and (d) show the intensity profiles of atomic lines centered on the Sr and Ti in STO averaged from (a) and (c), respectively.

FIG. 3. (Color online) (a) EEL spectra of Ti $L_{3,2}$-edge taken from STO bulk and the first to fourth TiO_2 layer near the STO/GaAs interface. The dashed lines denote the positions of the four peaks in the bulk spectrum. (b) O K-edge taken from STO bulk and the first to fourth SrO layer near the STO/GaAs interface. The spectrum data are smoothed using Gaussian function.

FIG. 4. (Color online) The computed ternary phase diagram of the formation energies of STO/GaAs interfaces with different stoichiometries under (a) Ga-rich ($\mu_{\mathrm{Ga}} = \mu_{\mathrm{Ga}}^{\mathrm{bulk}}$) and (b) As-rich ($\mu_{\mathrm{As}} = \mu_{\mathrm{As}}^{\mathrm{bulk}}$) conditions. The three axes are calculated as $\mu_{\mathrm{Sr}}^{*} = \mu_{\mathrm{Sr}} - \mu_{\mathrm{Sr}}^{\mathrm{bulk}}$, $\mu_{\mathrm{Ti}}^{*} = \mu_{\mathrm{Ti}} - \mu_{\mathrm{Ti}}^{\mathrm{bulk}}$ and $\mu_{\mathrm{O}}^{*} = \mu_{\mathrm{O}} - \frac{1}{2}\mu_{\mathrm{O_2}}^{\mathrm{molecule}}$, where $\mu_{\mathrm{Sr}}^{\mathrm{bulk}}$, $\mu_{\mathrm{Ti}}^{\mathrm{bulk}}$ and $\mu_{\mathrm{O_2}}^{\mathrm{molecule}}$ are approximated by their DFT total energies. The allowed chemical potential area of stable STO without formation of other bulk materials is bounded by the solid lines corresponding to the constraints of TiO_2, Ti_2O_3 and Ruddlesden-Popper structure $Sr_6Ti_5O_{16}$. The region to the right of the red line denotes the formation of Ga_2O_3.

FIG. 5. (Color online) The DFT-optimized structures of SrO/Ga and Sr/As interfaces. (a) The (2×2) SrO/Ga interface viewed in STO [010]||GaAs [110] and STO [100]||GaAs [$1\bar{1}0$] directions. (b) A (4×4) view of the reconstructed GaAs (001) surface at the SrO/Ga interface with the top Ga atoms highlighted. The unit cell of $c(2 \times 2)$ reconstruction is marked by red square. (c) The (2×2) Sr/As interface viewed in STO [010]||GaAs [110] and STO [100]||GaAs [$1\bar{1}0$] directions. (d) A (4×4) view of the unreconstructed GaAs (001) surface at the Sr/As interface.

FIG. 6. (Color online) Projected DOS on each element from the first to fourth STO and GaAs unit cells for (a) SrO/Ga interface and (b) Sr/As interface. The yellow, purple, green, blue and red curves represent DOS on Ga, As, Sr, Ti and O, respectively. Fermi level is shifted to zero and the energy gaps near Fermi level are marked by the shaded areas.

FIG. 7. (Color online) Charge density of Ti d_{xy} and $d_{yz} + d_{xz}$ occupied states at the CBM of STO as a function the distance of TiO_2 layers from the interface.

FIG. 8. (Color online) Band alignment diagrams of STO/GaAs hetero-structures for (a) SrO/Ga interface and (b) Sr/As interface. The blue solid curve represents the profile of electrostatic potential of the hetero-structure along out-of-plane direction $V(z)$, and the purple dashed curve represents the macroscopic average of the electrostatic potential. The red lines indicate the averaged values of the potential in bulk-like regions and the band alignment results. The conduction and valence band offsets are determined as $\Delta E_{\rm c} = E_{\rm c}^{\rm GaAs} - E_{\rm c}^{\rm STO}$ and $\Delta E_{\rm v} = E_{\rm v}^{\rm GaAs} - E_{\rm v}^{\rm STO}$. ΔV stands for the difference of the averaged potential between GaAs and STO parts.

FIG. 9. (Color online) Projected DOS on each element in the first STO and GaAs unit cells for the defect-induced interfaces. Fermi level is shifted to zero. $SrO/As_{0.5}$ is semiconducting with band gap marked by the shaded red area.

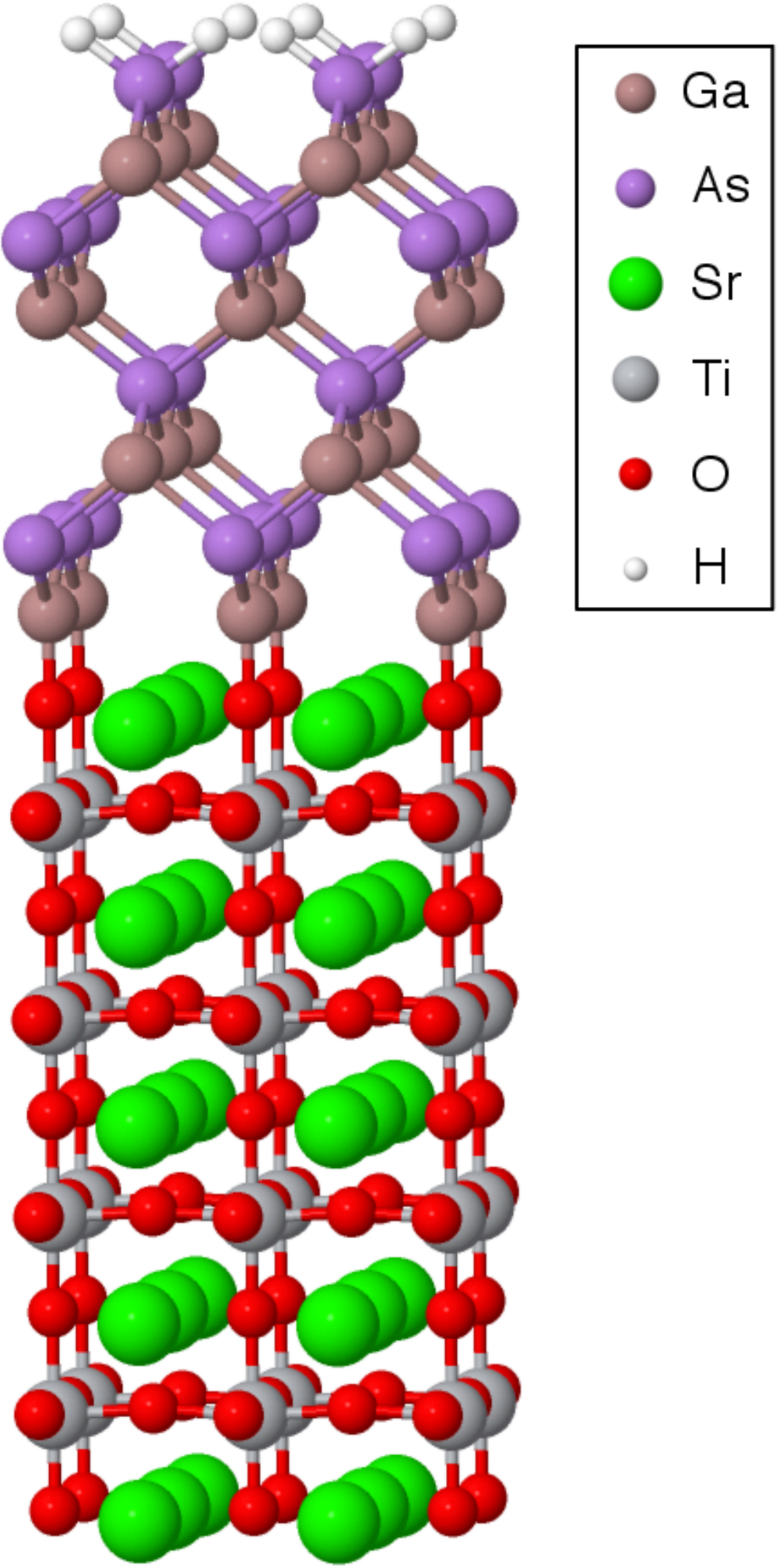
Ga
As
Sr
Ti
O
H

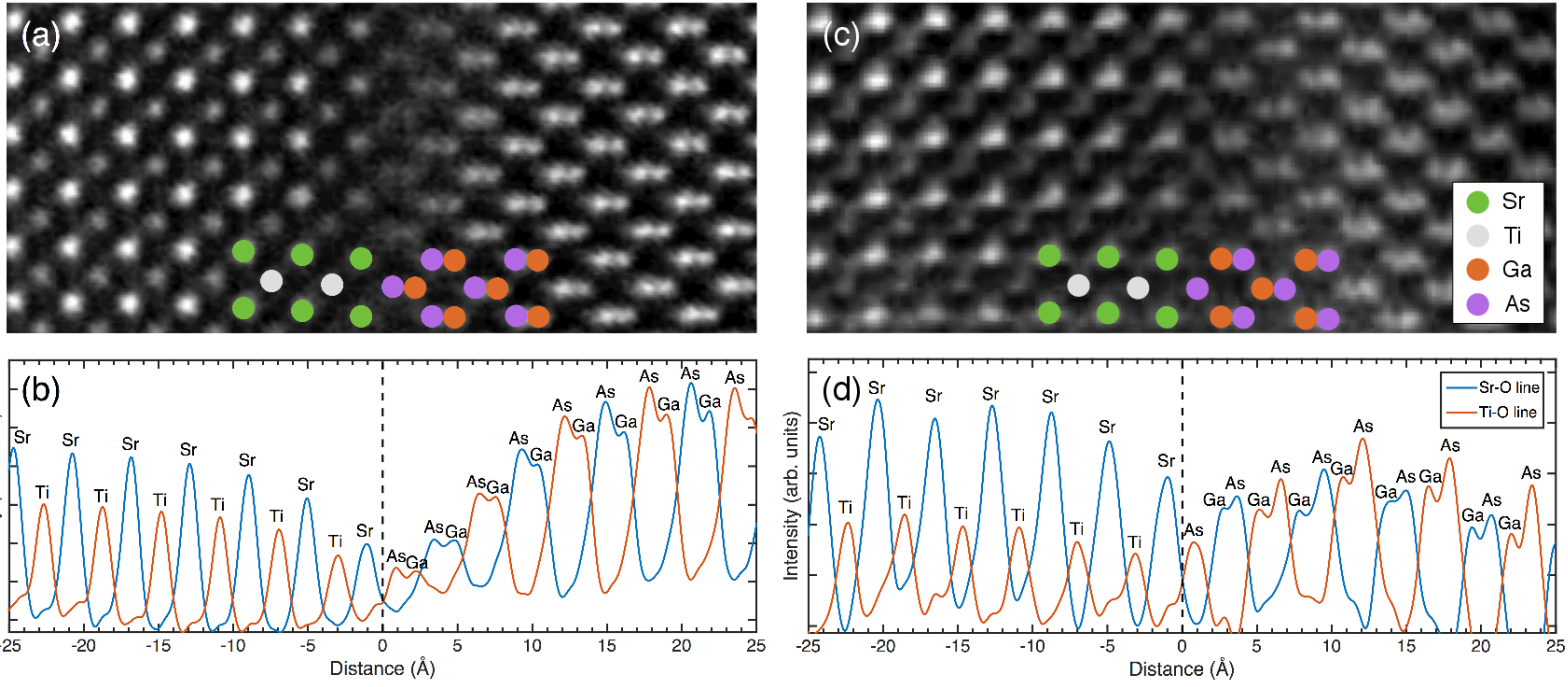
(a)
(c)
Sr
Ti
Ga
As
(b)
(d)
Intensity (arb. units)
Distance (Å)
Sr-O line
Ti-O line

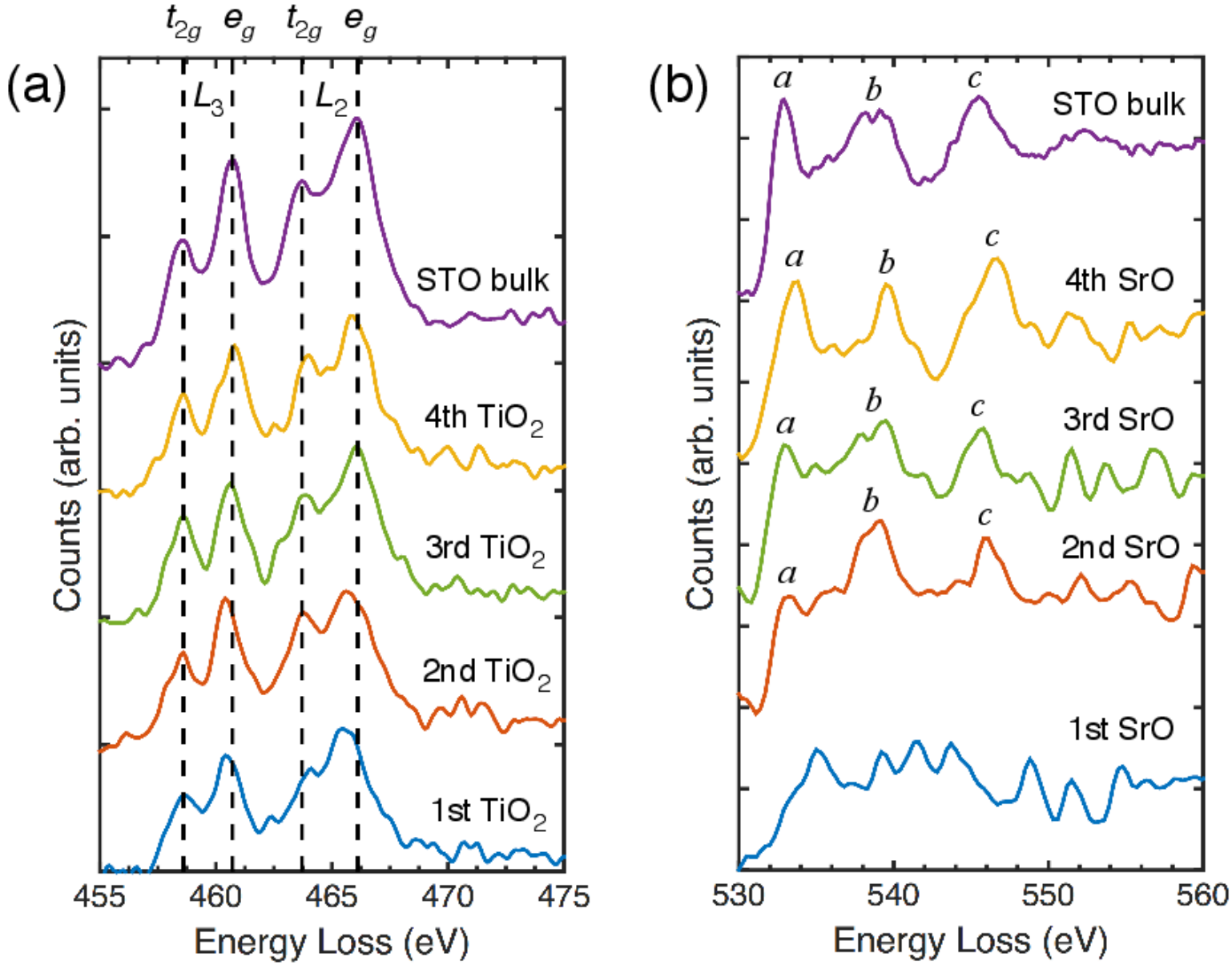
(a)
t_{2g} e_g t_{2g} e_g
L_3
L_2
STO bulk
4th TiO_2
3rd TiO_2
2nd TiO_2
1st TiO_2
Counts (arb. units)
455
460
465
470
475
Energy Loss (eV)
(b)
a
b
c
STO bulk
4th SrO
3rd SrO
2nd SrO
1st SrO
Counts (arb. units)
530
540
550
560
Energy Loss (eV)

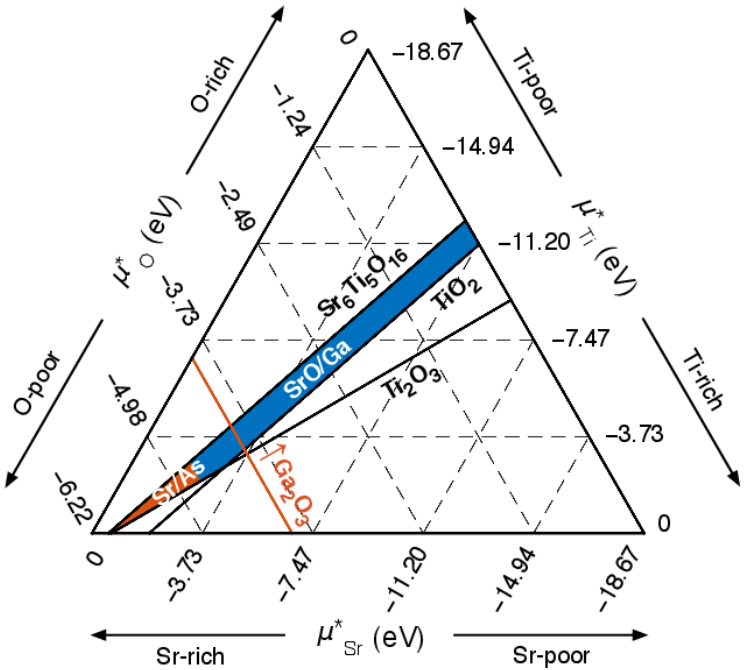

(a) Ga-rich

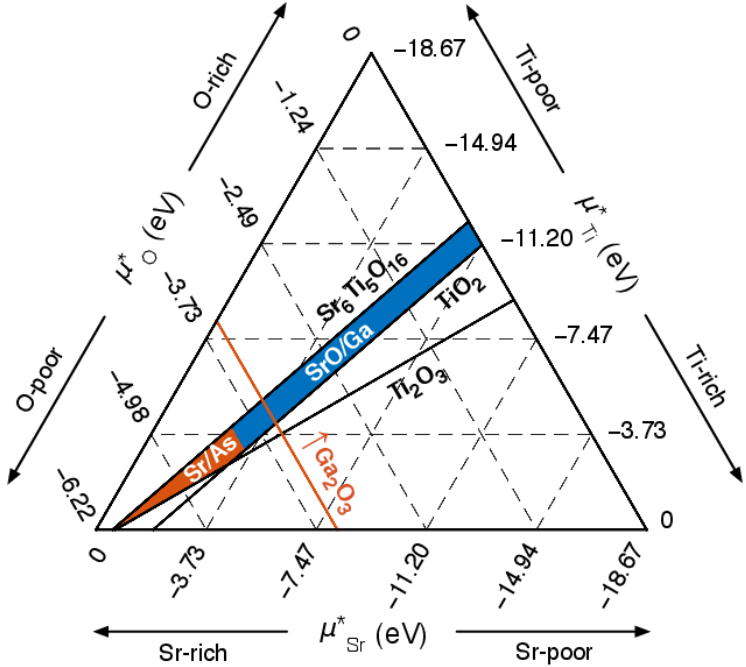

(b) As-rich

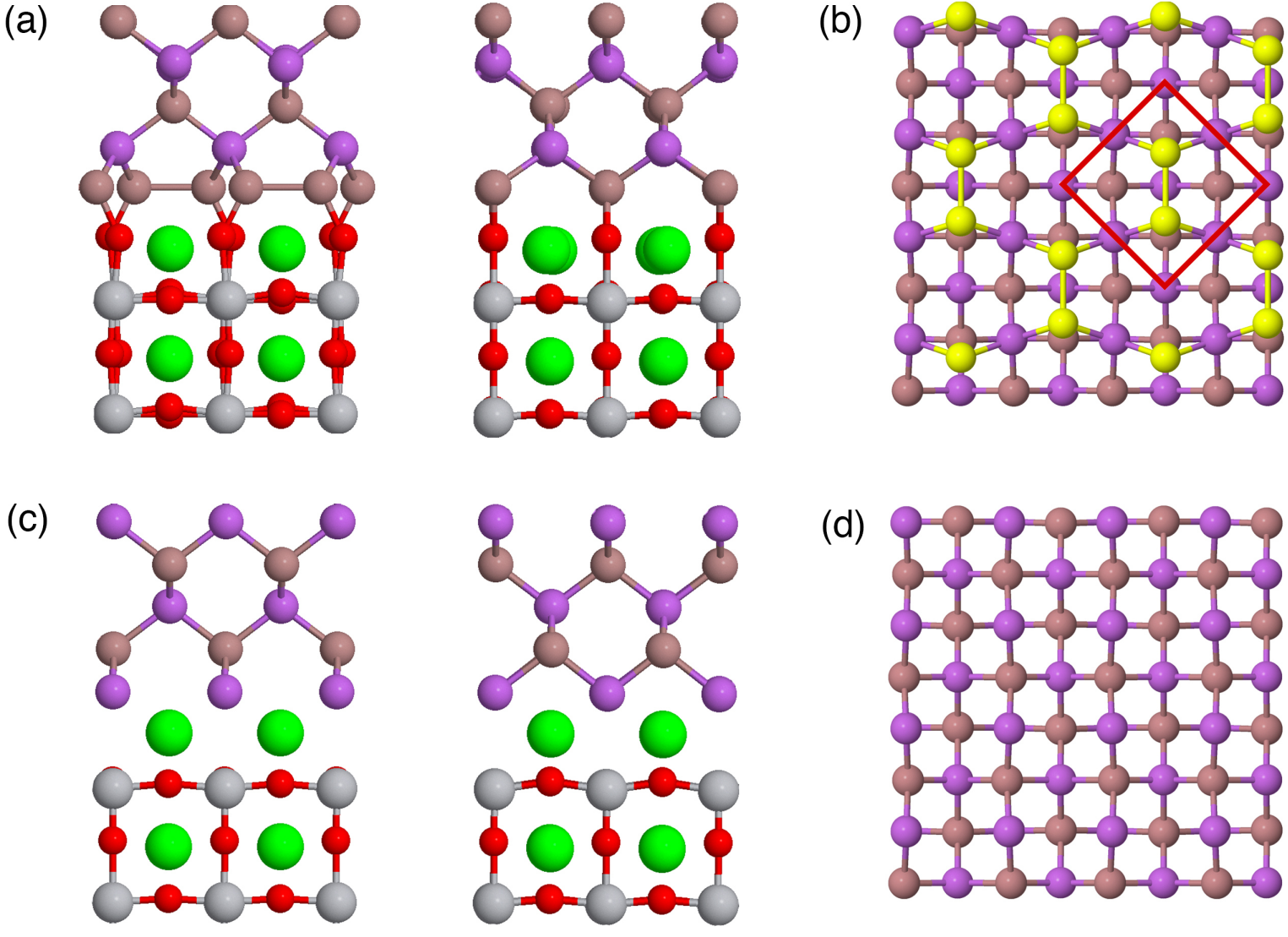
(a)
(b)
(c)
(d)

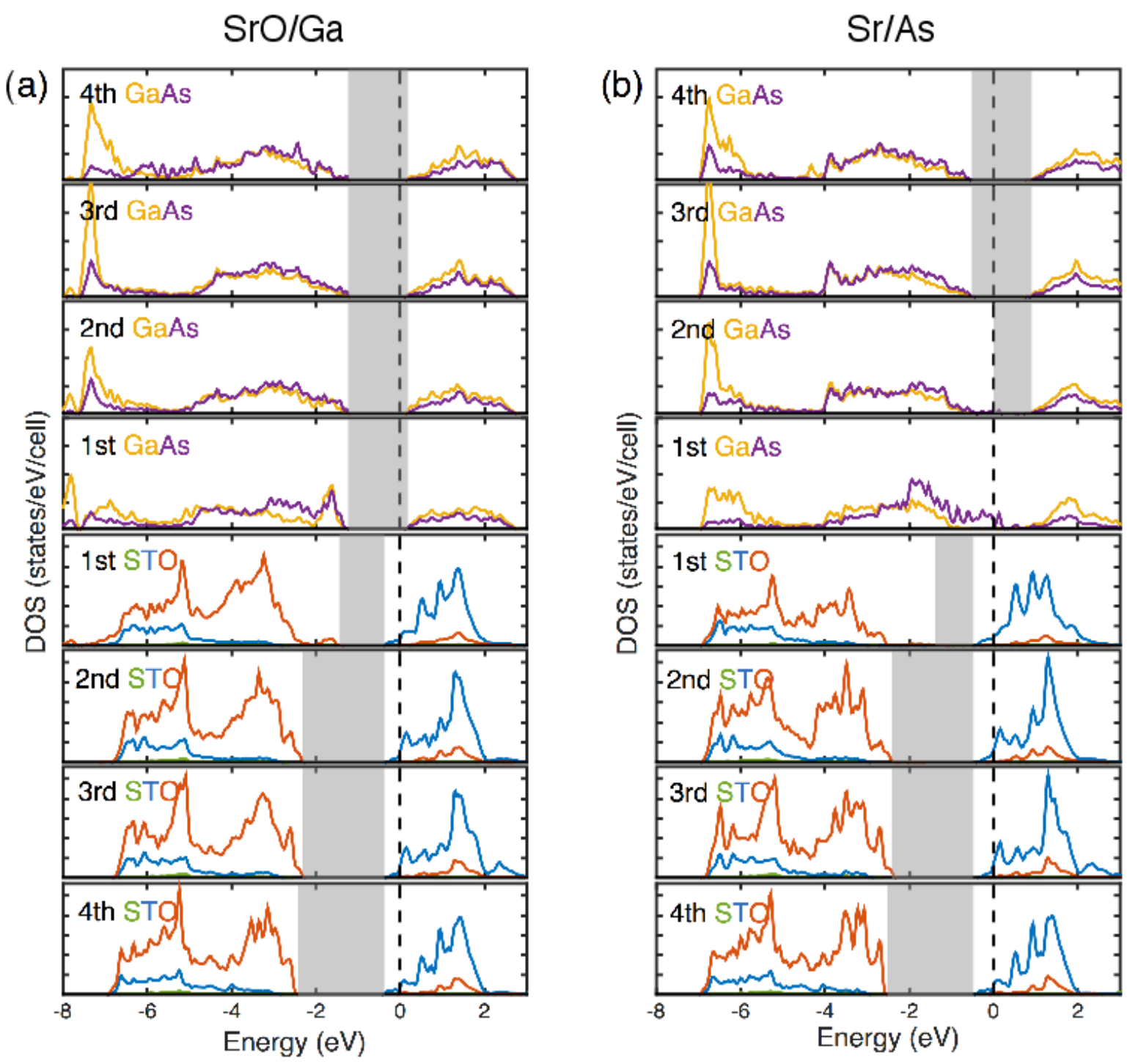
SrO/Ga
Sr/As
(a)
(b)
4th GaAs
3rd GaAs
2nd GaAs
1st GaAs
1st STO
2nd STO
3rd STO
4th STO
DOS (states/eV/cell)
Energy (eV)
-8
-6
-4
-2
0
2

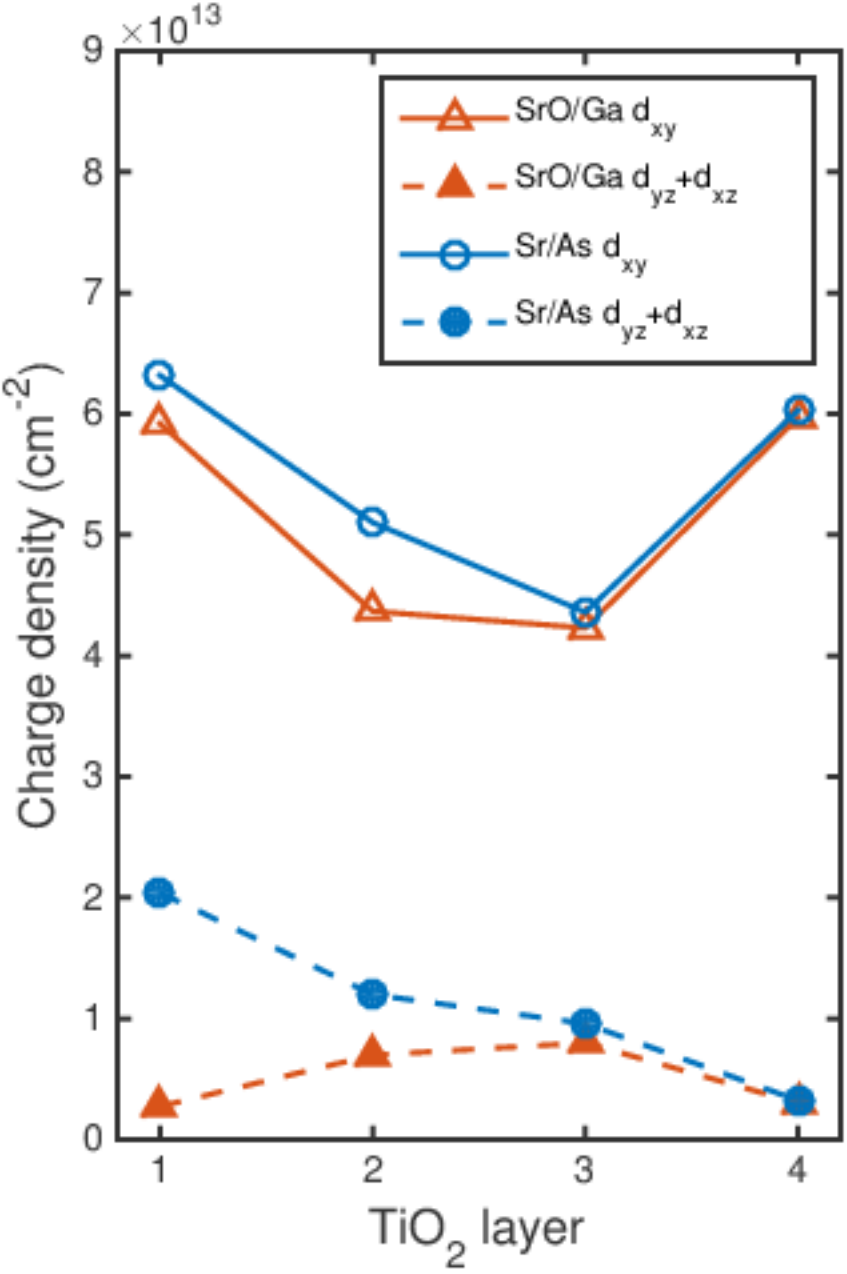
×10^13
9
8
7
6
5
4
3
2
1
0
Charge density (cm^-2)
1
2
3
4
TiO2 layer
SrO/Ga dxy
SrO/Ga dyz+dxz
Sr/As dxy
Sr/As dyz+dxz

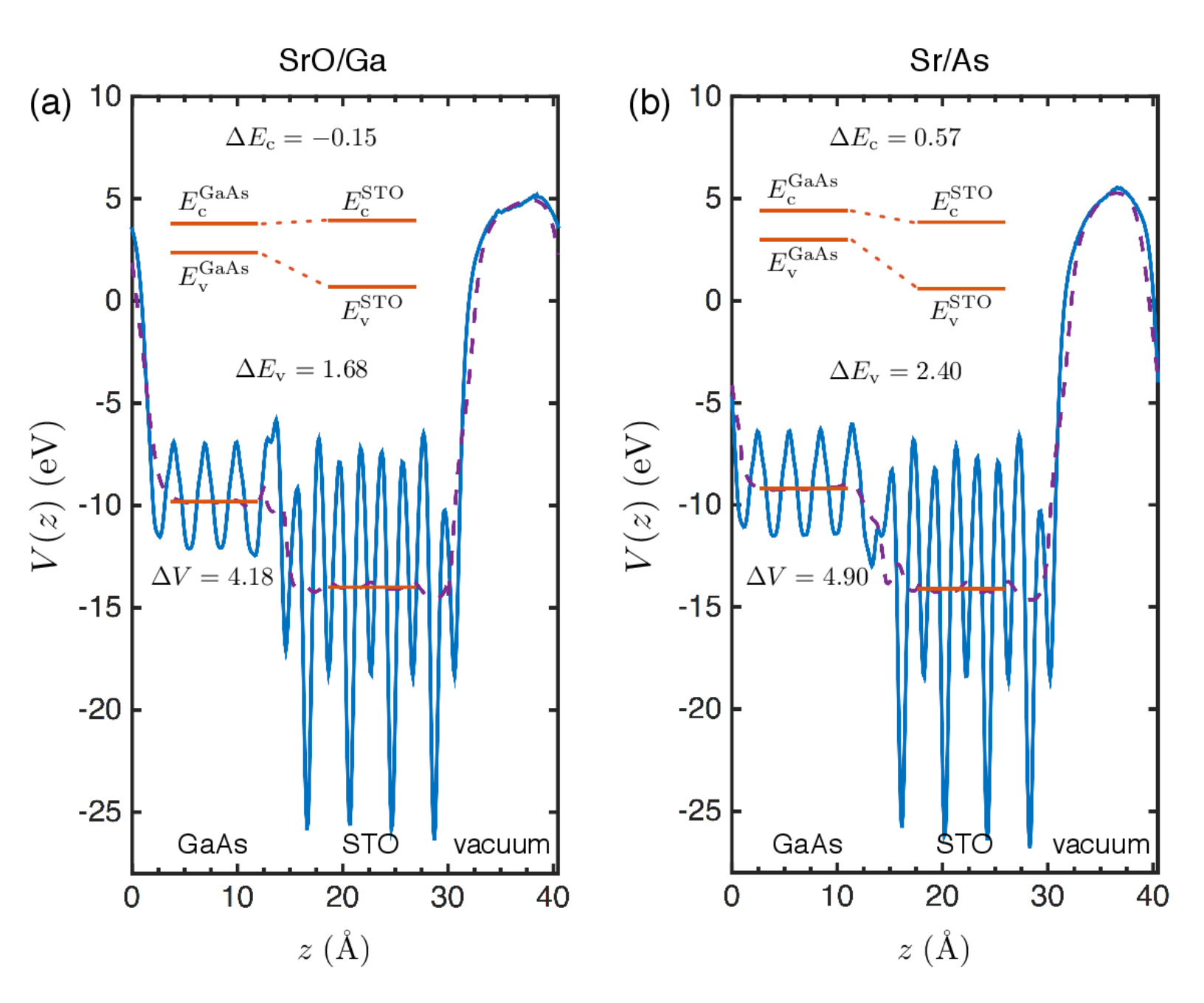
SrO/Ga
(a)
$\Delta E_c = -0.15$
E_c^{GaAs}
E_c^{STO}
E_v^{GaAs}
E_v^{STO}
$\Delta E_v = 1.68$
$\Delta V = 4.18$
GaAs
STO
vacuum
$V(z)$ (eV)
z (Å)
Sr/As
(b)
$\Delta E_c = 0.57$
E_c^{GaAs}
E_c^{STO}
E_v^{GaAs}
E_v^{STO}
$\Delta E_v = 2.40$
$\Delta V = 4.90$
GaAs
STO
vacuum
$V(z)$ (eV)
z (Å)

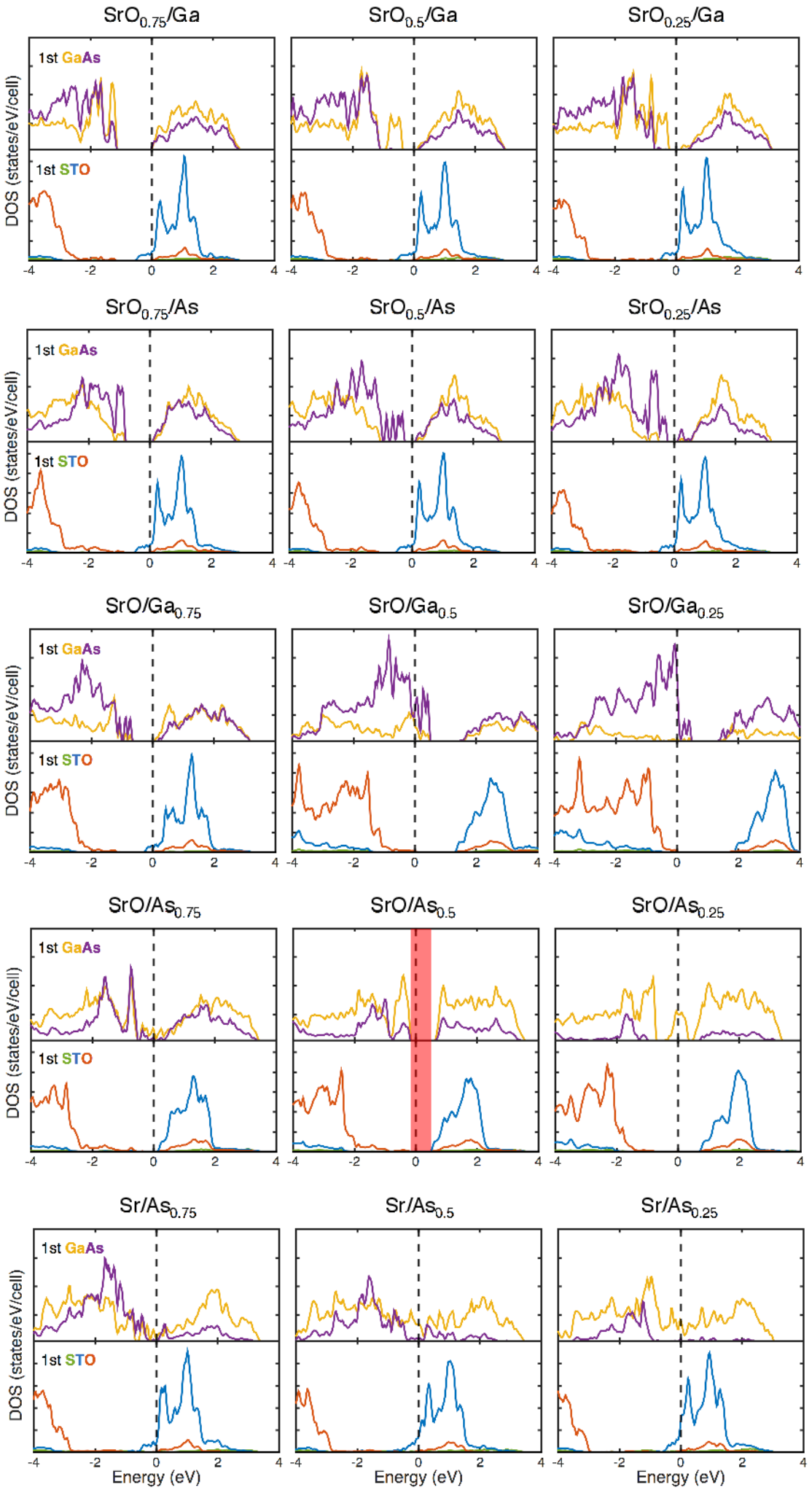
SrO0.75/Ga
SrO0.5/Ga
SrO0.25/Ga
SrO0.75/As
SrO0.5/As
SrO0.25/As
SrO/Ga0.75
SrO/Ga0.5
SrO/Ga0.25
SrO/As0.75
SrO/As0.5
SrO/As0.25
Sr/As0.75
Sr/As0.5
Sr/As0.25
1st GaAs
1st STO
DOS (states/eV/cell)
Energy (eV)
-4
-2
0
2
4